

Observation of correlated plasmons in low-valence nickelates

Y. Shen^{1, 2, 3, *}, W. He^{1, 4}, J. Sears¹, Xuefei Guo¹, Xiangpeng Luo¹, A. Roll¹,
 J. Li⁵, J. Pelliciari⁶, Xi He¹, I. Božović^{1, 6, †}, Junjie Zhang^{7, 8}, J. F. Mitchell⁷,
 V. Bisogni⁵, M. Mitrano⁹, S. Johnston^{10, 11} and M. P. M. Dean^{1, 10, ‡}

¹*Condensed Matter Physics and Materials Science Department,
 Brookhaven National Laboratory, Upton, New York 11973, USA*

²*Beijing National Laboratory for Condensed Matter Physics,
 Institute of Physics, Chinese Academy of Sciences, Beijing 100190, China*

³*School of Physical Sciences, University of Chinese Academy of Sciences, Beijing 100049, China*

⁴*Stanford Institute for Materials and Energy Sciences,
 SLAC National Accelerator Laboratory, Menlo Park, CA 94025, USA*

⁵*National Synchrotron Light Source II, Brookhaven National Laboratory, Upton, New York 11973, USA*

⁶*Department of Chemistry, Yale University, New Haven, Connecticut 06520, USA*

⁷*Materials Science Division, Argonne National Laboratory, Lemont, Illinois 60439, USA*

⁸*State Key Laboratory of Crystal Materials, Institute of Crystal Materials,
 Shandong University, Jinan, Shandong 250100, China*

⁹*Department of Physics, Harvard University, Cambridge, Massachusetts 02138, USA*

¹⁰*Department of Physics and Astronomy, The University of Tennessee, Knoxville, Tennessee 37966, USA*

¹¹*Institute of Advanced Materials and Manufacturing, The University of Tennessee, Knoxville, Tennessee 37996, USA*

(Dated: January 21, 2026)

The discovery of nickelate superconductors has opened a new arena for studying the behavior of correlated electron liquids that give rise to unconventional superconductivity. While critical information about a material's charge dynamics is encoded in its plasmons, collective modes of the electron gas, these excitations have not yet been observed in nickelate materials. Here, we use resonant inelastic x-ray scattering (RIXS) to detect plasmons in the metallic, low-valence nickelate $\text{Pr}_4\text{Ni}_3\text{O}_8$. Although qualitatively similar to those in cuprates, the nickelate plasmons are more heavily damped and have a lower velocity than those in a cuprate at comparable doping, which we attribute to reduced electronic hopping and enhanced screening of the long-range Coulomb interactions. Furthermore, the plasmons in $\text{Pr}_4\text{Ni}_3\text{O}_8$ soften with increasing temperature, in contrast to the cuprate, where plasmons remain at nearly fixed energy but become more strongly damped. Taken together, these results reveal a distinct charge-screening landscape in nickelates and place quantitative constraints on analogies to cuprates.

I. INTRODUCTION

The discovery of superconductivity in nickelates crowns decades of efforts to realize cuprate-like physics in materials that do not contain copper [1–5]. Two distinct subclasses of nickelates have been identified thus far: low-valence nickelates with formula $R_{n+1}\text{Ni}_n\text{O}_{2n+2}$ (where R is a rare earth and n denotes the number of neighboring layers) [6–10], and Ruddlesden-Popper (RP) phase nickelates with formula $R_{n+1}\text{Ni}_n\text{O}_{3n+1}$ [11–15]. Whereas the RP phases exhibit disparate band topology, the low-valence nickelates have band structures that share notable similarities with those of the cuprates, such as comparable electron counts [5, 16–18]. However, low-valence nickelates possess a larger charge-transfer energy compared to cuprates, placing them further from the charge-transfer regime [19] and correspondingly reducing their magnetic exchange interactions [20–26].

Although much is now known about nickelate band structures, it remains crucial to understand the dynamical properties of their normal state. These depend sensitively on the strength of the electron interactions and in particular screened Coulomb interactions, which are difficult to quantify from band structure measurements. This gap presents a compelling opportunity: recent studies indicate that attractive extended-Hubbard interactions—likely phonon-mediated—can promote superconductivity, but only if they are strong enough to overcome the long-range Coulomb repulsion [30–33]. Quantifying the magnitude of this Coulomb interaction is therefore essential. These Coulomb interactions manifest in plasmon excitations, which are the collective charge-density oscillations of low-energy electrons [34–37]. Plasmons have been studied extensively in cuprates [28, 29, 34, 38–46], but they are yet to be observed in nickelates. Filling this gap is imperative to directly compare screened interactions in nickelates and cuprates, and to identify universal features that are key to the formation of unconventional superconductivity.

Plasmons are traditionally measured using techniques such as optics and electron energy loss spectroscopy (EELS) [38, 47], but resonant inelastic x-ray scattering (RIXS) has emerged as an alternative [28, 29, 39–46]. It

* yshen@iphy.ac.cn

† [Shanghai Advanced Research in Physical Sciences \(SHARPS\),
 Pudong, Shanghai 201203, China](http://sharps.academy)

‡ mdean@bnl.gov

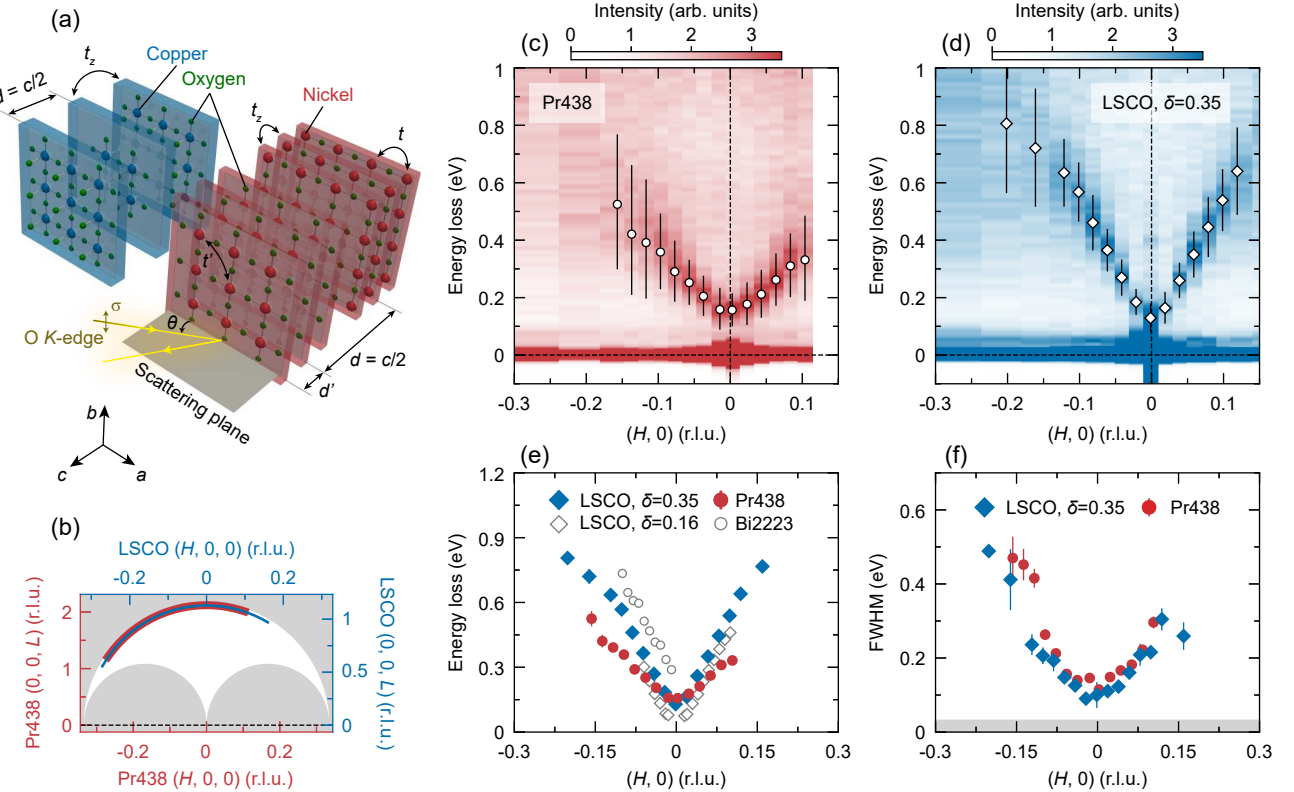


FIG. 1. Dispersive plasmons in Pr₄Ni₃O₈. (a), Schematic of the crystal structures of Pr₄Ni₃O₈ (Pr438, red) and La_{2-x}Sr_xCuO₄ (LSCO, blue), along with the corresponding structural and electronic hopping parameters. For the single layer model, d is the interlayer distance, and t_z denotes the interlayer electronic hopping integral. For the trilayer model, d and d' are the interlayer and intra-trilayer distances, respectively. t_z denotes the intra-trilayer hopping, while inter-trilayer hopping is neglected, as it is expected to be much smaller than the intra-trilayer term. t and t' are the nearest- and next-nearest-neighbor in-plane hopping for both Pr₄Ni₃O₈ and La_{2-x}Sr_xCuO₄. (b), Reciprocal space trajectories of the resonant inelastic x-ray scattering (RIXS) measurements of the in-plane plasmon dispersions, which were performed at a fixed scattering angle 2Θ . The values presented are in r.l.u. (reciprocal lattice units). (c),(d), RIXS intensity maps of Pr₄Ni₃O₈ and La_{2-x}Sr_xCuO₄ ($\delta = 0.35$), respectively, collected at 40 K, exhibiting dispersive plasmons with momenta primarily along the $(H, 0)$ direction, following the \mathbf{Q} trajectories presented in (b). The markers indicate plasmon peak positions extracted from fitting (See Ref. [27] Sec. S2). (e),(f) Summary of the in-plane plasmon dispersions, showing the peak positions and full-width at half-maximum (FWHM) that we obtain from fitting. Data for La_{2-x}Sr_xCuO₄ ($\delta = 0.16$) and Bi₂Sr₂Ca₂Cu₃O_{10+x} (Bi2223, $\delta = 0.18$) are reproduced from Ref. [28] and Ref. [29], respectively. The shaded area in (f) represents the quasi-elastic regime, determined by the energy resolution of ~ 30 meV. The full extent of the error bars in (c),(d) denote the full-width at half-maximum (FWHM) of plasmon peaks, whereas all other error bars are $1-\sigma$ confidence intervals evaluated from the fitting.

is especially useful for accessing the out-of-plane momentum dependence [28, 40], which is important because collective charge excitations in layered materials often disperse strongly along this direction, and the lowest-energy modes typically occur at finite momentum.

Here, we use O K -edge RIXS to study the plasmon excitations in single crystalline low-valence nickelate Pr₄Ni₃O₈, which we compare with overdoped cuprate La_{2-x}Sr_xCuO₄ with a similar effective hole-doping level. The nickelate exhibits well-defined dispersive plasmons at small in-plane momenta, which become overdamped well before crossing the particle-hole continuum inferred from the band structure. The plasmons in Pr₄Ni₃O₈ exhibit a reduced velocity compared to cuprates, indicating suppressed electronic hopping, and a broader

linewidth, suggestive of more strongly screened long-range Coulomb interactions. Our random phase approximation (RPA) calculations corroborate these observations, which also account for the lack of clear out-of-plane plasmon dispersion in Pr₄Ni₃O₈. We further observe that the plasmons in Pr₄Ni₃O₈ soften with increasing temperature, contrasting sharply with La_{2-x}Sr_xCuO₄, where they maintain their excitation energy but experience increased damping at elevated temperatures. Our findings reveal fundamental differences in charge dynamics between nickelate and cuprate superconductors, providing critical experimental constraints for identifying parameters essential to unconventional superconductivity.

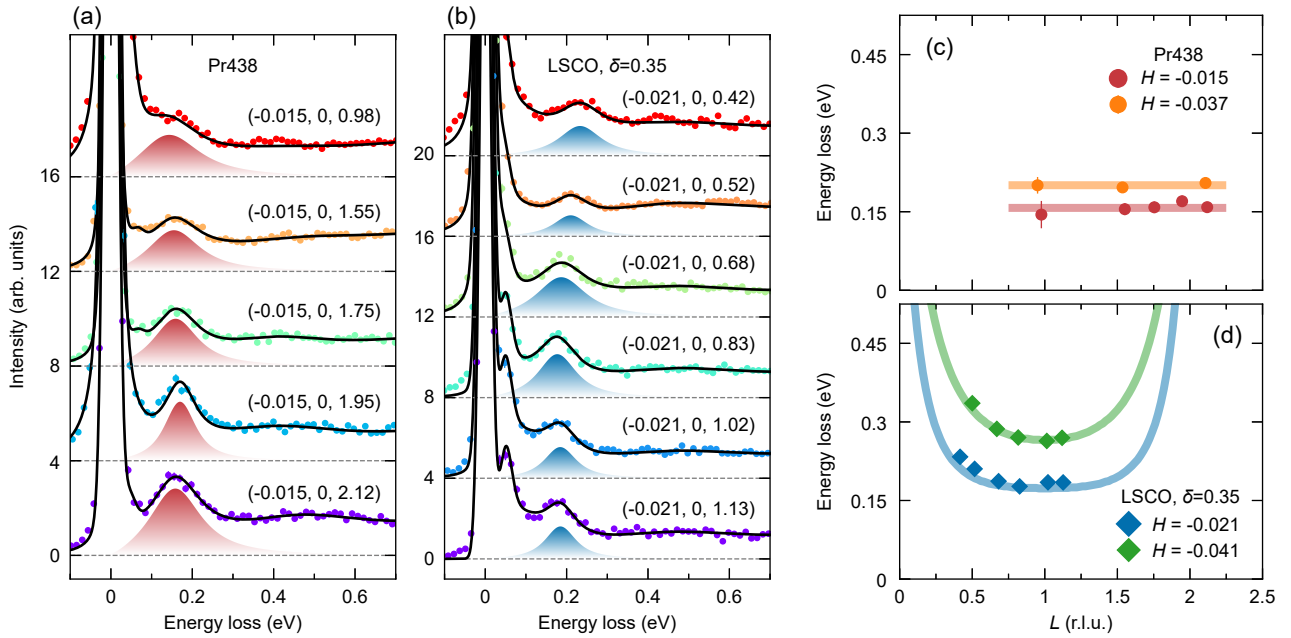


FIG. 2. Out-of-plane plasmon dispersions. (a),(b), RIXS spectra of various \mathbf{Q} along the out-of-plane L direction for $\text{Pr}_4\text{Ni}_3\text{O}_8$ and $\text{La}_{2-x}\text{Sr}_x\text{CuO}_4$ ($\delta = 0.35$), respectively. The shaded peak profiles represent the fitted plasmon contributions, and the solid black lines indicate the fitting results with all components accounted for, including the quasi-elastic line, low-energy phonons, and high-energy bimagnons combined with a continuous charge background. (c), Fitted plasmon peak positions of $\text{Pr}_4\text{Ni}_3\text{O}_8$. (d), Fitted plasmon peak positions of $\text{La}_{2-x}\text{Sr}_x\text{CuO}_4$. The solid lines are guides to the eye.

II. OBSERVATION OF DISPERSING PLASMONS IN NICKELATES

We choose $\text{Pr}_4\text{Ni}_3\text{O}_8$ as our reference low-valence nickelate [Fig. 1(a)] for this study and prepared samples via floating-zone growth, followed by topotactic reduction (see Sec. A). This material possesses a $\text{Ni } 3d^{9-1/3}$ valence state, corresponding to $\delta = 1/3$ hole doping with respect to the $3d^9$ parent state, placing it within the overdoped regime [48]. Distinct from its counterpart $\text{La}_4\text{Ni}_3\text{O}_8$, which undergoes a semiconductor-insulator transition accompanied by intertwined charge and spin order [49, 50], $\text{Pr}_4\text{Ni}_3\text{O}_8$ remains metallic down to 2 K with no identifiable phase transitions [48].

We begin by identifying the plasmon and mapping out its momentum dependence at 40 K. O K -edge RIXS data were collected as detailed in Sec. B. Figure 1(c),(d) display the RIXS energy-momentum maps for $\text{Pr}_4\text{Ni}_3\text{O}_8$ and $\text{La}_{2-x}\text{Sr}_x\text{CuO}_4$ ($\delta = 0.35$), respectively, along the $(H, 0)$ direction. The resonant condition for these measurements was determined by scanning the incident x-ray energy through the O K -edge pre-peak and identifying the energy that maximizes the intensity of the low-energy electronic excitations (see Ref. [27] Sec. S1). Both materials exhibit well-defined dispersive modes below 1 eV energy loss, which are widely recognized as plasmons in cuprate superconductors [28, 29, 40–46], as will be further verified by calculations presented later in this work. In electron-doped cuprates, as the doped electrons primar-

ily populate the upper Hubbard band of Cu $3d$ orbitals, the charge near the Fermi level exhibits dominant Cu $3d$ character. Consequently, plasmons are prominently observed at the Cu L edge in RIXS [40, 46]. In contrast, the doped carriers in hole-doped cuprates tend to occupy the ligand oxygen orbitals, making plasmons barely detectable at the Cu L edge but substantial at the O K edge [28, 46]. The clear observation of plasmon excitations in $\text{Pr}_4\text{Ni}_3\text{O}_8$ therefore implies an appreciable hole density on oxygen sites, supporting the observed mixed charge-transfer–Mott–Hubbard character of low-valence nickelates [23, 24].

Compared to the cuprate, $\text{Pr}_4\text{Ni}_3\text{O}_8$ exhibits plasmons with a lower energy scale and reduced dispersion slope [Fig. 1(e)], indicating a lower velocity and thus weakened electronic hopping. This distinction persists for lower dopings (for example $\text{La}_{2-x}\text{Sr}_x\text{CuO}_4$ $\delta = 0.16$) and in trilayer cuprates, as seen in Fig. 1(e). Plasmons in both $\text{Pr}_4\text{Ni}_3\text{O}_8$ and $\text{La}_{2-x}\text{Sr}_x\text{CuO}_4$ are heavily damped across reciprocal space, evidenced by peak widths exceeding the energy resolution of 30 meV [Fig. 1(f)], with the damping of the nickelate plasmon systematically exceeding that of the cuprate. In both cases the damping increases strongly with momentum and with the nickelate disappearing more quickly with momentum than the cuprate.

A key characteristic of cuprate plasmons is their out-of-plane periodic dispersion highlighting the importance of interlayer coupling beyond the typically assumed two-dimensional (2D) framework for cuprates [28, 40]. Fig-

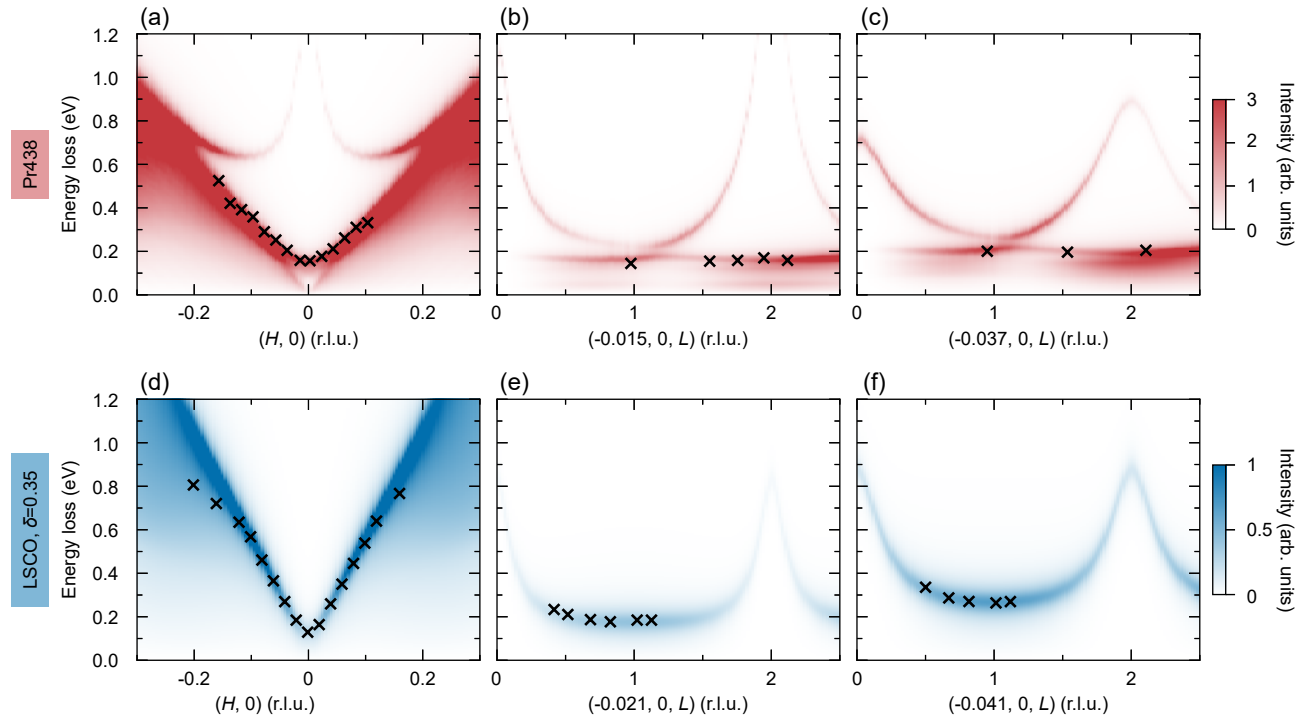


FIG. 3. Theoretical description of the dispersing plasmons. (a)–(c), Simulations of plasmons in $\text{Pr}_4\text{Ni}_3\text{O}_8$ based on RPA calculations of the dynamical susceptibility applied to a trilayer model, as described in the main text. (d)–(f), RPA simulations of plasmons in $\text{La}_{2-x}\text{Sr}_x\text{CuO}_4$ ($\delta = 0.35$) applied to a single-layer model. The crosses represent plasmon peak positions derived from fitting the experimental data. In (a) and (d), the simulations followed the experimental \mathbf{Q} trajectory as shown in Fig. 1(b), while in other panels, the in-plane momentum transfer H was fixed at the indicated values.

TABLE I. Parameters describing plasmons in the two materials. Here, t , t' , and t_z are electronic hopping integrals, as defined in Fig. 1(a), and V_c is the long-range Coulomb interaction with its spatial anisotropy controlled by α . Note that μ is the chemical potential while $\Delta\mu$ is the potential difference between the outer and inner layers of the trilayer model. Full details are provided in Sec. C&D.

Material	t (eV)	t'/t	t' (eV)	t_z/t	t_z (eV)	α	V_c/t	V_c (eV)	μ (eV)	$\Delta\mu/t$	$\Delta\mu$ (eV)
LSCO ($\delta = 0.35$)	0.39	-0.3	-0.117	0.017	0.00663	3.5	15	5.85	-0.51	–	–
Pr438	0.21	-0.3	-0.063	0.04	0.0084	–	6	1.26	-0.28	-0.4	-0.084

ure 2 summarizes the out-of-plane dispersion. As expected, our $\text{La}_{2-x}\text{Sr}_x\text{CuO}_4$ ($\delta = 0.35$) RIXS data reveal clear dispersive plasmons along the out-of-plane direction [Fig. 2(b),(d)], matching earlier reports. In contrast, $\text{Pr}_4\text{Ni}_3\text{O}_8$ exhibits no resolvable out-of-plane plasmon dispersion over a \mathbf{Q} range spanning the full anticipated period [Fig. 2(a),(c)]. Similar behavior was observed in a trilayer cuprate, which was attributed to out-of-phase plasmon oscillations that become undetectable by RIXS [29]. Therefore, the lack of out-of-plane plasmon dispersion likely reflects the presence of three coupled planes in $\text{Pr}_4\text{Ni}_3\text{O}_8$, rather than indicating a fundamental difference in the interactions.

III. THEORETICAL DESCRIPTION OF THE DISPERSING PLASMONS

To better understand the implications of our observations, and quantify changes in hopping and screening in these materials, we simulated the plasmons using RPA calculations of the charge dynamical susceptibility, which incorporates dynamically screened interactions arising from collective, mean-field-like density fluctuations. Further correlation effects beyond this approximation can be partly captured through parameter renormalization [46]. Such RPA simulations can therefore associate the differences in plasmon behavior between nickelates and cuprates with specific variations in the underlying interactions in the materials.

For $\text{La}_{2-x}\text{Sr}_x\text{CuO}_4$, we employ a single-layer model and consider anisotropic long-range Coulomb interac-

tions and intralayer/interlayer electronic hopping (Methods). Satisfactory agreement occurs using the parameters presented in Table I, which reproduce plasmon dispersions in both in-plane and out-of-plane directions [Fig. 3(d)–(f)].

For $\text{Pr}_4\text{Ni}_3\text{O}_8$, we construct a corresponding trilayer model using tight-binding parameters appropriate for the known band structure as determined by angle-resolved photoemission spectroscopy (ARPES) measurements [51], incorporating intra-trilayer hopping while neglecting inter-trilayer terms, as the former dominates (Methods). The simulations achieve reasonable agreement with experiment, as depicted in Fig. 3(a)–(c), using the parameters presented in Table I. Notably, $\text{Pr}_4\text{Ni}_3\text{O}_8$ exhibits substantially reduced in-plane hopping and long-range Coulomb interaction V_c compared to $\text{La}_{2-x}\text{Sr}_x\text{CuO}_4$ ($\delta = 0.35$), consistent with the reduced plasmon velocity of $1.2 \pm 0.1 \text{ eV}\text{\AA}$ compared to $2.4 \pm 0.2 \text{ eV}\text{\AA}$ in the cuprate [Figs. 1(c),(d)], linking the observed changes in plasmon velocity to changes in the underlying Hamiltonian. Meanwhile, the intra-trilayer hopping in $\text{Pr}_4\text{Ni}_3\text{O}_8$ is larger than the interlayer hopping in $\text{La}_{2-x}\text{Sr}_x\text{CuO}_4$ due to its reduced interlayer distance, despite the absence of apical oxygens [Fig. 1(a)].

Although simulations of the charge dynamical susceptibility predict multiple plasmon modes [Fig. 3(a)–(c)], only one mode is experimentally resolved. For most \mathbf{Q} vectors, the upper branches are predicted either to have intensities below the RIXS detection threshold ($L < 0.4$) or to merge into the high-energy charge continuum ($L \sim 2$), making them hard to distinguish from the background [29, 45, 52, 53]. However, at specific \mathbf{Q} vectors like those in Fig. 3(c) with $L \sim 1.5$, RPA predicts that plasmon branches stay well-separated at low energies, with sufficient intensity for detection; yet they remain unobserved in the experiment. Thus, alternative mechanisms need to be considered. One possibility is that matrix element effects suppress these modes in the RIXS process. More sophisticated multi-orbital calculations, taking into account the full Kramers-Heisenberg cross-section would be needed to address this possibility. Another more likely possibility is that these modes are obscured by correlations beyond those captured in standard RPA calculations. For example, self-energy broadening, which becomes increasingly pronounced as the quasiparticle energy shifts away from the Fermi level [51], can broaden the higher-energy plasmon branches significantly, exceeding observability, while the lower-energy modes remain coherent. This scenario is supported by RPA simulations incorporating phenomenological energy-dependent self-energy broadening (Ref. [27] Fig. S7).

IV. TEMPERATURE DEPENDENCE

Having established a qualitative picture of low-temperature plasmons, we now explore their response to thermal fluctuations. Figure 4 presents temperature-

dependent RIXS measurements and the corresponding fitting results. For $\text{La}_{2-x}\text{Sr}_x\text{CuO}_4$ ($\delta = 0.35$), plasmon excitation energy remains nearly constant while the profile broadens with increasing temperature, consistent with prior reports [44]. In contrast, plasmons in $\text{Pr}_4\text{Ni}_3\text{O}_8$ soften at higher temperatures while maintaining similar peak widths (Fig. 4).

The lower plasmon velocity in $\text{Pr}_4\text{Ni}_3\text{O}_8$ reflects greater electronic compressibility and thus an increased susceptibility to charge order in conditions where this instability is energetically favored. These novel plasmon effects are intriguing in light of prior evidence of incipient stripe order in $\text{Pr}_4\text{Ni}_3\text{O}_8$ [18, 22, 54]. Since studies of the related material $\text{La}_4\text{Ni}_3\text{O}_8$ show that stripe order modifies the material's electrical conductivity and consequently the plasmon screening [48, 49], stripe fluctuations are a possible candidate for the temperature dependence of the plasmon.

V. IMPLICATIONS OF NICKELATE CHARGE DYNAMICS

Our results provide the first measurements of dispersive plasmons in low-valence nickelate $\text{Pr}_4\text{Ni}_3\text{O}_8$ and compare them with those in $\text{La}_{2-x}\text{Sr}_x\text{CuO}_4$ with a similar doping level. The plasmon velocity, indicated by the dispersion slope in Fig. 1(e), is found to be smaller in $\text{Pr}_4\text{Ni}_3\text{O}_8$ than $\text{La}_{2-x}\text{Sr}_x\text{CuO}_4$ implying reduced electronic hopping in the former. Prior experimental and theoretical work has shown that $\text{Pr}_4\text{Ni}_3\text{O}_8$ shares similar electronic properties to other low valence nickelates, provided that they are compared at the same effective doping [22–24, 55, 56], so this trend of suppressed electronic hopping and enhanced screening is likely to be a general property of low valence nickelates compared to the cuprates.

At first glance, the trend in the plasmon velocities is perhaps surprising as the nominally Ni^{1+} site in nickelates hosts a smaller nuclear charge than the Cu^{2+} site in cuprates and so it would be expected to have more extended transition-metal (TM) d -orbitals and *larger* hopping. Indeed, prior works have found that the TM-O hopping values in the low-valence nickelates exhibit are larger, or at least similar to the values found in cuprates [23, 55]. Instead, the difference in the plasmon dispersion can be explained by the fact that the transfer energy is also larger in low-valence nickelates, so the effective TM-TM hopping bridged by oxygen is weaker. The more extended Ni orbitals are also likely to increase screening and have a role in the smaller long-range Coulomb interaction, which is almost a factor of five smaller in the nickelate compared to the cuprate.

Another notable feature of the plasmons observed here is that they are more heavily damped and disappear at smaller values of in-plane momentum compared to the cuprate. In a simple uncorrelated metal, plasmons become heavily damped only once their momentum crosses

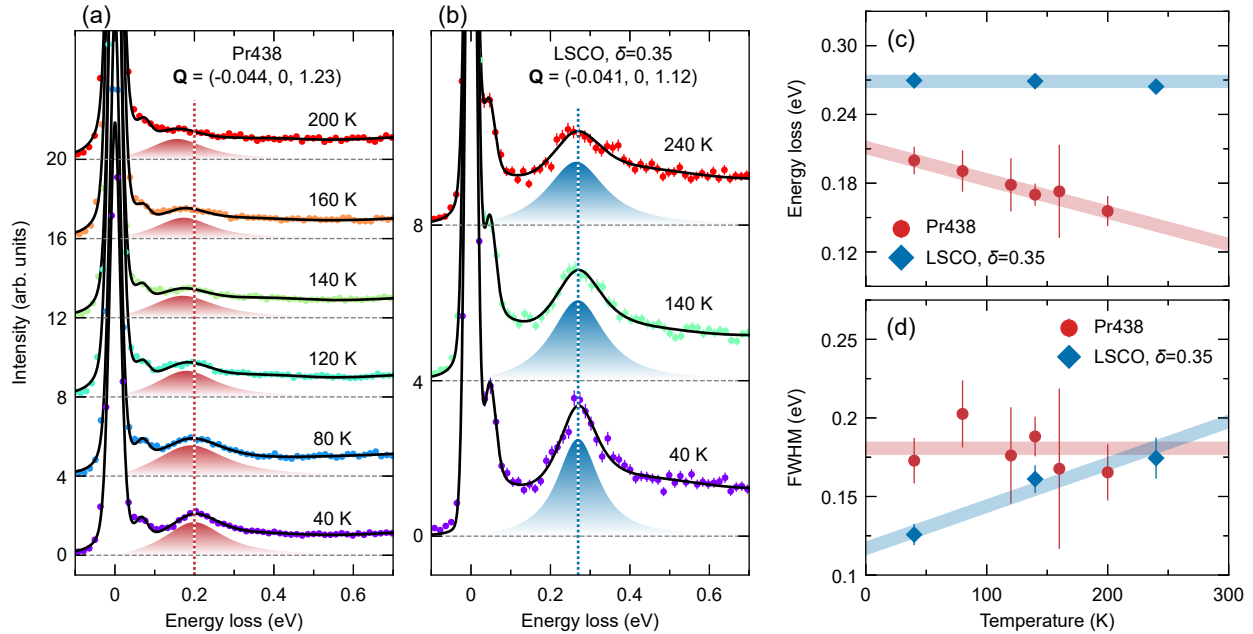


FIG. 4. Temperature dependence of the plasmons. (a),(b), Temperature dependent RIXS spectra for $\text{Pr}_4\text{Ni}_3\text{O}_8$ and $\text{La}_{2-x}\text{Sr}_x\text{CuO}_4$ ($\delta = 0.35$), respectively, collected at the indicated \mathbf{Q} vectors and temperatures. The shaded areas indicate the fitted plasmon profiles, and the black lines denote the summation of different contributions. (c),(d), Temperature dependence of the plasmon peak positions and FWHM, respectively, obtained from the fitting. The dashed lines in (a),(b) and bold lines in (c),(d) are guides to the eye.

the particle-hole continuum. Indeed, the implications of the anomalous damping of cuprate plasmons has been discussed extensively [28, 57, 58] and the microscopic origin of this damping remains controversial. Possible explanations range from strange metal physics in which plasmons decay into a quantum critical continuum [59], or by interband transitions, which effectively extend the Landau damping regime [60]. We find that this anomalous plasmon damping is even stronger in nickelates, which can shed further light on this problem. The temperature dependence of the nickelate plasmon also appears to be anomalous, exhibiting a strong softening with increased temperature that may be connected to stripe correlations.

Overall, our findings establish reduced electronic hopping and smaller, more strongly screened, long-range Coulomb interactions as defining features differentiating low-valence nickelates from cuprates. These differences could ultimately lead to a suppression of the superconducting energy scale [61], providing a possible explanation for the lower T_c in low-valence nickelates compared to cuprates. These results offer essential experimental benchmarks for contrasting low-valence nickelates and cuprates, guiding efforts toward realizing unconventional superconductivity with higher transition temperatures.

ACKNOWLEDGMENTS

We thank Mike Norman, Hiroyuki Yamase, Andres Greco, Matias Bejas, and Peter Abbamonte for discussions. Work at Brookhaven and the University of Tennessee (RIXS measurements and the interpretation and model Hamiltonian calculations) was supported by the U.S. Department of Energy, Office of Science, Office of Basic Energy Sciences, under Award Number DE-SC0022311. Work at Harvard was supported by the U.S. Department of Energy, Office of Science, Office of Basic Energy Sciences, under Award Number DE-SC0012704. Work at Argonne (nickelate sample synthesis) was supported by the U.S. DOE, Office of Science, Basic Energy Sciences, Materials Science and Engineering Division. Y.S. acknowledges support by the National Key R&D Program of China (Grant No. 2024YFA1408301). J.Z. was supported by the National Natural Science Foundation of China (Grants Nos. 12074219 and 12374457). This research used resources at the SIX beamline of the National Synchrotron Light Source II, a U.S. DOE Office of Science User Facility operated for the DOE Office of Science by Brookhaven National Laboratory under Contract No. DE-SC0012704.

DATA AVAILABILITY

The RIXS data generated in this study have been deposited in the Zenodo database under accession code [to be assigned].

Appendix A: Sample synthesis

The parent RP phase $\text{Pr}_4\text{Ni}_3\text{O}_{10}$ material was synthesized via the high-pressure optical floating zone method. To reduce the samples, small c -axis-surface-normal crystals were cleaved from the boules and heated in a flowing H_2/Ar gas mixture following previously reported procedures [48]. We use tetragonal notation with space group $I4/mmm$ and lattice constants of $a = b = 3.935 \text{ \AA}$, $c = 25.485 \text{ \AA}$ to describe reciprocal space. The intra-trilayer spacing $d' = 3.185 \text{ \AA}$ and the inter-trilayer distance is $d = c/2 = 12.74 \text{ \AA}$. The excellent quality of the samples was confirmed by previous studies [22–25].

The $\text{La}_{2-x}\text{Sr}_x\text{CuO}_4$ film used in the current study was synthesized using the atomic-layer-by-layer molecular beam epitaxy (ALL-MBE) technique [62]. Prior studies of samples prepared via ALL-MBE have confirmed the high sample quality [23, 63–65]. The lattice constants of $\text{La}_{2-x}\text{Sr}_x\text{CuO}_4$ are $a = b \approx 3.76 \text{ \AA}$ and $c = 13.17 \text{ \AA}$. Layers are spaced by $d = c/26.8 \text{ \AA}$.

For both materials, momentum transfer is denoted using reciprocal lattice units (r.l.u.) notation as $\mathbf{Q} = H\mathbf{a}^* + K\mathbf{b}^* + L\mathbf{c}^*$.

Appendix B: RIXS measurements

High-energy-resolution RIXS measurements were performed at the SIX beamline at the National Synchrotron Light Source II (NSLS-II). All the RIXS data presented here were collected with incident σ polarization at the pre-peak of the O K edge, where the plasmon intensities are maximized (Supplementary Note 1). During the experiments, we put the crystalline ($H, 0, 0$) and $(0, 0, L)$ directions in the horizontal scattering plane [Fig. 1(a)]. The spectra were collected with an energy resolution of around 30 meV. A multi-peak fitting procedure was employed to extract the plasmon parameters, including the excitation energies and peak widths (Supplementary Note 2).

Appendix C: RPA calculations: Single layer model

In the single layer RPA calculations, we treat the electronic dispersion as $\epsilon_{\mathbf{k}} = \epsilon_{\mathbf{k}}^{\parallel} + \epsilon_{\mathbf{k}}^{\perp}$, where

$$\epsilon_{\mathbf{k}}^{\parallel} = -2t [\cos(k_x a) + \cos(k_y a)] - 4t' \cos(k_x a) \cos(k_y a) - \mu \quad (\text{C1})$$

and

$$\epsilon_{\mathbf{k}}^{\perp} = -2t_z [\cos(k_x a) - \cos(k_y a)]^2 \cos(k_z d) \quad (\text{C2})$$

are the dispersions parallel and perpendicular to the ab plane, respectively [44]. k_x and k_y denote the in-plane momenta, expressed in units of $2\pi/a$, while k_z represents the out-of-plane momentum in units of $2\pi/d$. Here, a is the in-plane lattice constant and d is defined in Fig. 1(a). The chemical potential μ is set by imposing $1 - \delta = \frac{2}{N} \sum_{\mathbf{k}} n_F(\epsilon_{\mathbf{k}})$, where δ is doping and $n_F(\epsilon_{\mathbf{k}}) = 1/[e^{(\epsilon_{\mathbf{k}} - \mu)\beta} + 1]$ is the Fermi function, $\beta = 1/k_B T$ is the inverse temperature, and N is the total number of sites [28]. Note that all the calculations were performed at $T = 40 \text{ K}$.

In the single layer case, the RPA charge susceptibility on the Matsubara frequency axis is given by

$$\chi(\mathbf{q}, i\omega_m) = \frac{\chi_0(\mathbf{q}, i\omega_m)}{1 - V(\mathbf{q})\chi_0(\mathbf{q}, i\omega_m)}, \quad (\text{C3})$$

where $\omega_m = 2m\pi/\beta$ is a bosonic Matsubara frequency,

$$\chi_0(\mathbf{q}, \omega_m) = \frac{2}{N\beta} \sum_{\mathbf{k}, n} G_0(\mathbf{k} + \mathbf{q}, i\omega_n + i\omega_m) G_0(\mathbf{k}, i\omega_n)$$

is the Lindhard susceptibility, $G_0(\mathbf{k}, i\omega_n) = 1/(i\omega_n - \epsilon_{\mathbf{k}})$ is the noninteracting Green's function, $\omega_n = (2n + 1)\pi/\beta$ is a fermionic Matsubara frequency, and

$$V(\mathbf{q}) = \frac{V_c}{\alpha[2 - \cos(q_x a) - \cos(q_y a)] + 1 - \cos(q_z d)} \quad (\text{C4})$$

is the long-range Coulomb interaction for a layered electron gas [28]. Here, α describes the anisotropy.

The imaginary part of the charge susceptibility on the real axis $\chi''(\mathbf{q}, \omega)$, which is the quantity we wish to compare to our measurements, can be obtained by analytical continuation $\chi(\mathbf{q}, i\omega_n \rightarrow \omega + i\gamma)$. In this case, the Lindhard function on the real frequency axis is given by

$$\chi_0(\mathbf{q}, \omega + i\gamma) = -\frac{2}{N} \sum_{\mathbf{k}} \frac{n_F(\mathbf{k} + \mathbf{q}) - n_F(\mathbf{k})}{\omega_n - \epsilon_{\mathbf{k} + \mathbf{q}} + \epsilon_{\mathbf{k}} + i\gamma}. \quad (\text{C5})$$

In our numerical calculations, we take $\gamma = 5 \text{ meV}$ to account for resolution broadening of the charge susceptibility. We further fix $\alpha = 3.5$ [28] and $t'/t = -0.3$ and tuned t_z/t and V_c/t to search for the best combination of parameters that can reproduce the $\text{La}_{2-x}\text{Sr}_x\text{CuO}_4$ ($\delta = 0.35$) plasmon dispersions (Ref. [27] Fig. S4). For a given combination of t_z/t and V_c/t , t can be uniquely determined as it controls the overall energy scale. The best fit parameters are given in Table I. Note that the change in plasmon dispersion resulting from reducing V_c can be partly compensated by increasing t , so we further use ARPES data to constrain the latter, obtaining a unique solution.

Appendix D: RPA calculations: Trilayer model

In the trilayer model, we use $d = 3.286a$ and $d' = 0.8215a$ to denote the out-of-plane inter- and intra-trilayer distances, respectively [see Fig. 1(a)]. As such the out-of-plane momentum is reported in units of $2\pi/d$.

We model the noninteracting electronic structure of the multilayer crystal using the Hamiltonian $H = \sum_{\mathbf{k},\sigma} \Psi_{\mathbf{k},\sigma}^\dagger \hat{h}_{\mathbf{k}} \Psi_{\mathbf{k},\sigma}$, where $\Psi_{\mathbf{k},\sigma}^\dagger = [c_{\mathbf{k},1,\sigma}^\dagger, c_{\mathbf{k},2,\sigma}^\dagger, c_{\mathbf{k},3,\sigma}^\dagger]$ is a row vector of operators $c_{\mathbf{k},\alpha,\sigma}^\dagger$ are creation operators for a spin σ electron in layer α and

$$\hat{h}_{\mathbf{k}} = \begin{pmatrix} \epsilon_{\mathbf{k}}^{\parallel} + \frac{\Delta\mu}{3} & \epsilon_{\mathbf{k}}^{\perp} & 0 \\ \epsilon_{\mathbf{k}}^{\perp*} & \epsilon_{\mathbf{k}}^{\parallel} - \frac{2\Delta\mu}{3} & \epsilon_{\mathbf{k}}^{\perp} \\ 0 & \epsilon_{\mathbf{k}}^{\perp*} & \epsilon_{\mathbf{k}}^{\parallel} + \frac{\Delta\mu}{3} \end{pmatrix}. \quad (\text{D1})$$

Here, $\Delta\mu$ is the potential difference between layers, which is introduced to account for inequivalent doping levels in the inner ($n = 2$) and outer ($n = 1, 3$) layers, as observed in ARPES measurements on $\text{Pr}_4\text{Ni}_3\text{O}_8$ [51]. The in-plane component of the dispersion $\epsilon_{\mathbf{k}}^{\parallel}$ is defined as in Eq. (C1) while the out-of-plane component is

$$\epsilon_{\mathbf{k}}^{\perp} = -2t_z[\cos(k_x a) - \cos(k_y a)]^2 e^{ik_z d'}. \quad (\text{D2})$$

The electronic dispersions in the band basis is obtained by diagonalizing $\hat{\epsilon}_{\mathbf{k}} = U_{\mathbf{k}}^\dagger \hat{h}_{\mathbf{k}} U_{\mathbf{k}}$, where $\hat{\epsilon}_{\mathbf{k}}$ is a diagonal matrix representing the eigenvalues of $\hat{h}_{\mathbf{k}}$.

The RPA susceptibility, written in the orbitals basis, is a 3×3 matrix given by

$$\chi(\mathbf{q}, i\omega_m) = [\mathbb{I} - V(\mathbf{q})\chi_0(\mathbf{q}, i\omega_m)]^{-1} \chi_0(\mathbf{q}, i\omega_m). \quad (\text{D3})$$

Here, \mathbb{I} is an identity matrix, $V(\mathbf{q})$ is the long-range Coulomb interaction for coupled sets of layered gases, and $\chi_0(\mathbf{q}, i\omega_m)$ is the Lindhard function, written in the layer basis. The Coulomb interaction is defined as [29]

$$V(\mathbf{q}) = \begin{pmatrix} V_{11} & V_{12} & V_{13} \\ V_{12}^* & V_{11} & V_{12} \\ V_{13}^* & V_{12}^* & V_{11} \end{pmatrix}, \quad (\text{D4})$$

where

$$\begin{aligned} V_{11}(\mathbf{q}) &= \frac{V_c}{\mathbf{q}_{\parallel}} \left(\frac{\sinh(|\mathbf{q}_{\parallel}|d)}{\cosh(|\mathbf{q}_{\parallel}|d) - \cos(q_z d)} \right) \\ V_{12}(\mathbf{q}) &= \frac{V_c}{\mathbf{q}_{\parallel}} \left(\frac{\sinh(|\mathbf{q}_{\parallel}|(d - d')) + e^{-iq_z d} \sinh(|\mathbf{q}_{\parallel}|d')}{\cosh(|\mathbf{q}_{\parallel}|d) - \cos(q_z d)} \right) e^{-iq_z d'} \\ V_{13}(\mathbf{q}) &= \frac{V_c}{\mathbf{q}_{\parallel}} \left(\frac{\sinh(|\mathbf{q}_{\parallel}|(d - 2d')) + e^{-iq_z d} \sinh(|\mathbf{q}_{\parallel}|2d')}{\cosh(|\mathbf{q}_{\parallel}|d) - \cos(q_z d)} \right) e^{-i2q_z d'}. \end{aligned} \quad (\text{D5})$$

The RIXS response is obtained from the imaginary part of the analytically continued RPA susceptibility [45]

$$\text{Im}\chi_c(\mathbf{q}, \omega) = -\sum_{\alpha, \beta} \text{Im}\chi_{\alpha, \beta}(\mathbf{q}, i\omega_m \rightarrow \omega + i\gamma). \quad (\text{D6})$$

The Lindhard function in this case is given by

$$\chi_{\alpha, \beta}^0(\mathbf{q}, \omega) = -\frac{2}{N} \sum_{\mathbf{k}, \mu, \nu} \int_{-\infty}^{\infty} dx \int_{-\infty}^{\infty} dy A_{\nu, \nu}(\mathbf{k} + \mathbf{q}, y) A_{\mu, \mu}(\mathbf{k}, y) U_{\mu, \alpha}(\mathbf{k}) U_{\mu, \beta}^*(\mathbf{k}) U_{\nu, \beta}(\mathbf{k} + \mathbf{q}) U_{\nu, \alpha}^*(\mathbf{k} + \mathbf{q}) \frac{n_{\text{F}}(y) - n_{\text{F}}(x)}{\omega - y + x + i\gamma},$$

where α and β are orbital indices and μ and ν are band indices and $A(\mathbf{k}, \omega) = -\frac{1}{\pi} \text{Im}G(\mathbf{k}, \omega)$ is the spectral function in the band basis.

In the noninteracting limit, the spectral function is diagonal with elements $A_{\nu, \nu}(\mathbf{k}, \omega) = \delta(\omega - \epsilon_{\nu}(\mathbf{k}))$, where $\epsilon_{\nu}(\mathbf{k})$ are the eigenvalues of Eq. (D1). In the interacting case, we assume that the self-energy is diagonal and has a Fermi-liquid-like dependence $\Sigma_{\nu, \nu}(\omega) = -i(\kappa_0 + \kappa\omega^2)$ such that $A_{\nu, \nu}(\mathbf{k}, \omega) = -\frac{1}{\pi} \text{Im}[\omega - \epsilon_{\nu}(\mathbf{k}) - \Sigma_{\nu, \nu}(\omega)]^{-1}$. Here, κ_0 and κ control the strength of the impurity scat-

tering and electron-electron scattering, respectively.

For our $\text{Pr}_4\text{Ni}_3\text{O}_8$ plasmon simulations, we fixed $t'/t = -0.3$, as in the single layer model, and adjusted t_z/t , V_c/t , and $\Delta\mu/t$ (see Ref. [27] Fig. S5). Similar to $\text{La}_{2-x}\text{Sr}_x\text{CuO}_4$, the change in plasmon dispersion by reducing V_c can be compensated by increasing t . Thus, we can use ARPES data to further constrain the latter

[51]. Meanwhile, the simulated Fermi surface also needs to match the experimental observations, which can help constrain t'/t and $\Delta\mu/t$ (Ref. [27] Fig. S6). It is also worth noting that the reduced t and V_c in $\text{Pr}_4\text{Ni}_3\text{O}_8$ com-

pared to $\text{La}_{2-x}\text{Sr}_x\text{CuO}_4$ can be concluded directly from a qualitative consideration of the RIXS data, thus the simulations act to confirm and quantify a trend already evident in the raw data.

[1] M. Crespin, P. Levitz, and L. Gatineau, Reduced forms of LaNiO_3 perovskite. part 1.—evidence for new phases: $\text{La}_2\text{Ni}_2\text{O}_5$ and LaNiO_2 , *J. Chem. Soc., Faraday Trans. 2* **79**, 1181 (1983).

[2] V. Anisimov, D. Bukhvalov, and T. Rice, Electronic structure of possible nickelate analogs to the cuprates, *Physical Review B* **59**, 7901 (1999).

[3] M. R. Norman, Entering the nickel age of superconductivity, *Physics* **13**, 85 (2020).

[4] J. Zhang and X. Tao, Review on quasi-2D square planar nickelates, *CrystEngComm.* **23**, 3249 (2021).

[5] B. Y. Wang, K. Lee, and B. H. Goodge, Experimental progress in superconducting nickelates, *Annual Review of Condensed Matter Physics* **15**, 305 (2024).

[6] D. Li, K. Lee, B. Y. Wang, M. Osada, S. Crossley, H. R. Lee, Y. Cui, Y. Hikita, and H. Y. Hwang, Superconductivity in an infinite-layer nickelate, *Nature* **572**, 624 (2019).

[7] G. A. Pan, D. Ferenc Segedin, H. LaBollita, Q. Song, E. M. Nica, B. H. Goodge, A. T. Pierce, S. Doyle, S. Novakov, D. Córdova Carrizales, *et al.*, Superconductivity in a quintuple-layer square-planar nickelate, *Nature Materials* **21**, 160 (2022).

[8] S. L. E. Chow, Z. Luo, and A. Ariando, Bulk superconductivity near 40 K in hole-doped SmNiO_2 at ambient pressure, *Nature* **642**, 58 (2025).

[9] M. Yang, H. Wang, J. Tang, J. Luo, X. Wu, R. Mao, W. Xu, G. Zhou, Z. Dong, B. Feng, L. Shi, Z. Pei, P. Gao, Z. Chen, and D. Li, Enhanced superconductivity in codoped infinite-layer samarium nickelate thin films (2025), [arXiv:arXiv:2503.18346 \[cond-mat\]](https://arxiv.org/abs/2503.18346).

[10] X. Yan, H. Zheng, Y. Li, H. Cao, D. P. Phelan, H. Zheng, Z. Zhang, H. Hong, G. Wang, Y. Liu, A. Bhattacharya, H. Zhou, and D. D. Fong, Superconductivity in an ultra-thin multilayer nickelate, *Science Advances* **11**, eado4572 (2025).

[11] H. Sun, M. Huo, X. Hu, J. Li, Z. Liu, Y. Han, L. Tang, Z. Mao, P. Yang, B. Wang, J. Cheng, D.-X. Yao, G.-M. Zhang, and M. Wang, Signatures of superconductivity near 80 K in a nickelate under high pressure, *Nature* **621**, 493 (2023).

[12] Y. Zhu, D. Peng, E. Zhang, B. Pan, X. Chen, L. Chen, H. Ren, F. Liu, Y. Hao, N. Li, Z. Xing, F. Lan, J. Han, J. Wang, D. Jia, H. Wo, Y. Gu, Y. Gu, L. Ji, W. Wang, H. Gou, Y. Shen, T. Ying, X. Chen, W. Yang, H. Cao, C. Zheng, Q. Zeng, J.-g. Guo, and J. Zhao, Superconductivity in pressurized trilayer $\text{La}_4\text{Ni}_3\text{O}_{10-\delta}$ single crystals, *Nature* **631**, 531 (2024).

[13] E. K. Ko, Y. Yu, Y. Liu, L. Bhatt, J. Li, V. Thampy, C.-T. Kuo, B. Y. Wang, Y. Lee, K. Lee, J.-S. Lee, B. H. Goodge, D. A. Muller, and H. Y. Hwang, Signatures of ambient pressure superconductivity in thin film $\text{La}_3\text{Ni}_2\text{O}_7$, *Nature* **638**, 935 (2025).

[14] G. Zhou, W. Lv, H. Wang, Z. Nie, Y. Chen, Y. Li, H. Huang, W.-Q. Chen, Y.-J. Sun, Q.-K. Xue,

[15] M. Shi, D. Peng, K. Fan, Z. Xing, S. Yang, Y. Wang, H. Li, R. Wu, M. Du, B. Ge, Z. Zeng, Q. Zeng, J. Ying, T. Wu, and X. Chen, Pressure induced superconductivity in hybrid Ruddlesden–Popper $\text{La}_5\text{Ni}_3\text{O}_{11}$ single crystals, *Nature Physics* **21**, 1780 (2025).

[16] Y. Nomura and R. Arita, Superconductivity in infinite-layer nickelates, *Reports on Progress in Physics* **85**, 052501 (2022).

[17] K. Lee, B. Y. Wang, M. Osada, B. H. Goodge, T. C. Wang, Y. Lee, S. Harvey, W. J. Kim, Y. Yu, C. Murthy, S. Raghu, L. F. Kourkoutis, and H. Y. Hwang, Linear-in-temperature resistivity for optimally superconducting $(\text{Nd},\text{Sr})\text{NiO}_2$, *Nature* **619**, 288 (2023).

[18] M. Hepting, M. P. M. Dean, and W.-S. Lee, Soft x-ray spectroscopy of low-valence nickelates, *Frontiers in Physics* **9**, 10.3389/fphy.2021.808683 (2021).

[19] J. Zaanen, G. A. Sawatzky, and J. W. Allen, Band gaps and electronic structure of transition-metal compounds, *Physical Review Letters* **55**, 418 (1985).

[20] M. Hepting, D. Li, C. Jia, H. Lu, E. Paris, Y. Tseng, X. Feng, M. Osada, E. Been, Y. Hikita, *et al.*, Electronic structure of the parent compound of superconducting infinite-layer nickelates, *Nature Materials* **19**, 381 (2020).

[21] H. Lu, M. Rossi, A. Nag, M. Osada, D. F. Li, K. Lee, B. Y. Wang, M. Garcia-Fernandez, S. Agrestini, Z. X. Shen, E. M. Been, B. Moritz, T. P. Devoreaux, J. Zaanen, H. Y. Hwang, K.-J. Zhou, and W. S. Lee, Magnetic excitations in infinite-layer nickelates, *Science* **373**, 213 (2021).

[22] J. Q. Lin, P. Villar Arribi, G. Fabbris, A. S. Botana, D. Meyers, H. Miao, Y. Shen, D. G. Mazzzone, J. Feng, S. G. Chiuzbăian, A. Nag, A. C. Walters, M. García-Fernández, K.-J. Zhou, J. Pelliciari, I. Jarrige, J. W. Freeland, J. Zhang, J. F. Mitchell, V. Bisogni, X. Liu, M. R. Norman, and M. P. M. Dean, Strong superexchange in a $d^{9-\delta}$ nickelate revealed by resonant inelastic x-ray scattering, *Physical Review Letters* **126**, 087001 (2021).

[23] Y. Shen, J. Sears, G. Fabbris, J. Li, J. Pelliciari, I. Jarrige, X. He, I. Božović, M. Mitrano, J. Zhang, J. F. Mitchell, A. S. Botana, V. Bisogni, M. R. Norman, S. Johnston, and M. P. M. Dean, Role of oxygen states in the low valence nickelate $\text{La}_4\text{Ni}_3\text{O}_8$, *Physical Review X* **12**, 011055 (2022).

[24] Y. Shen, J. Sears, G. Fabbris, J. Li, J. Pelliciari, M. Mitrano, W. He, J. Zhang, J. F. Mitchell, V. Bisogni, M. R. Norman, S. Johnston, and M. P. M. Dean, Electronic character of charge order in square-planar low-valence nickelates, *Physical Review X* **13**, 011021 (2023).

[25] G. Fabbris, D. Meyers, Y. Shen, V. Bisogni, J. Zhang, J. Mitchell, M. Norman, S. Johnston, J. Feng, G. Chiuzbăian, A. Nicolaou, N. Jaouen, and M. Dean, Resonant

inelastic x-ray scattering data for ruddlesden-popper and reduced ruddlesden-popper nickelates, *Scientific Data* **10**, 174 (2023).

[26] M. R. Norman, A. S. Botana, J. Karp, A. Hampel, H. LaBollita, A. J. Millis, G. Fabbris, Y. Shen, and M. P. M. Dean, Orbital polarization, charge transfer, and fluorescence in reduced-valence nickelates, *Physical Review B* **107**, 165124 (2023).

[27] See Supplemental Material at [URL will be inserted by publisher] for further details of the plasmon resonance and data fitting.

[28] A. Nag, M. Zhu, M. Bejas, J. Li, H. C. Robarts, H. Yamase, A. N. Petsch, D. Song, H. Eisaki, A. C. Walters, M. García-Fernández, A. Greco, S. M. Hayden, and K.-J. Zhou, Detection of acoustic plasmons in hole-doped lanthanum and bismuth cuprate superconductors using resonant inelastic x-ray scattering, *Physical Review Letters* **125**, 257002 (2020).

[29] S. Nakata, M. Bejas, J. Okamoto, K. Yamamoto, D. Shiga, R. Takahashi, H. Y. Huang, H. Kumigashira, H. Wadati, J. Miyawaki, S. Ishida, H. Eisaki, A. Fujimori, A. Greco, H. Yamase, D. J. Huang, and H. Suzuki, Out-of-phase plasmon excitations in the trilayer cuprate $\text{Bi}_2\text{Sr}_2\text{Ca}_2\text{Cu}_3\text{O}_{10+\delta}$, *Physical Review B* **111**, 165141 (2025).

[30] Z. Chen, Y. Wang, S. N. Rebec, T. Jia, M. Hashimoto, D. Lu, B. Moritz, R. G. Moore, T. P. Devereaux, and Z.-X. Shen, Anomalously strong near-neighbor attraction in doped 1d cuprate chains, *Science* **373**, 1235 (2021).

[31] M. Jiang, Enhancing d -wave superconductivity with nearest-neighbor attraction in the extended hubbard model, *Physical Review B* **105**, 024510 (2022).

[32] H. Padma, J. Thomas, S. F. R. TenHuisen, W. He, Z. Guan, J. Li, B. Lee, Y. Wang, S. H. Lee, Z. Mao, H. Jang, V. Bisogni, J. Pelliciari, M. P. M. Dean, S. Johnston, and M. Mitrano, Beyond-hubbard pairing in a cuprate ladder, *Physical Review X* **15**, 021049 (2025).

[33] A. Scheie, P. Laurell, J. Thomas, V. Sharma, A. I. Kolesnikov, G. E. Granroth, Q. Zhang, B. Lake, M. M. Jr., R. I. Bewley, R. S. Eccleston, J. Akimitsu, E. Dagotto, C. D. Batista, G. Alvarez, S. Johnston, and D. A. Tennant, Cooper-pair localization in the magnetic dynamics of a cuprate ladder (2025), arXiv:2501.10296 [cond-mat.str-el].

[34] I. Bozovic, Plasmons in cuprate superconductors, *Physical Review B* **42**, 1969 (1990).

[35] A. Foussats and A. Greco, Large- N expansion based on the hubbard operator path integral representation and its application to the $t - J$ model. II. the case for finite J , *Physical Review B* **70**, 205123 (2004).

[36] A. Greco, H. Yamase, and M. Bejas, Plasmon excitations in layered high- T_c cuprates, *Physical Review B* **94**, 075139 (2016).

[37] L. Zinni, M. Bejas, H. Yamase, and A. Greco, Low-energy plasmon excitations in infinite-layer nickelates, *Physical Review B* **107**, 014503 (2023).

[38] P. Abbamonte and J. Fink, Collective charge excitations studied by electron energy-loss spectroscopy, *Annual Review of Condensed Matter Physics* **16**, 465 (2025).

[39] M. Mitrano, S. Johnston, Y.-J. Kim, and M. P. M. Dean, Exploring quantum materials with resonant inelastic x-ray scattering, *Physical Review X* **14**, 040501 (2024).

[40] M. Hepting, L. Chaix, E. W. Huang, R. Fumagalli, Y. Y. Peng, B. Moritz, K. Kummer, N. B. Brookes, W. C. Lee, M. Hashimoto, T. Sarkar, J.-F. He, C. R. Rotundu, Y. S. Lee, R. L. Greene, L. Braicovich, G. Ghiringhelli, Z. X. Shen, T. P. Devereaux, and W. S. Lee, Three-dimensional collective charge excitations in electron-doped copper oxide superconductors, *Nature* **563**, 374 (2018).

[41] J. Lin, J. Yuan, K. Jin, Z. Yin, G. Li, K.-J. Zhou, X. Lu, M. Dantz, T. Schmitt, H. Ding, H. Guo, M. P. M. Dean, and X. Liu, Doping evolution of the charge excitations and electron correlations in electron-doped superconducting $\text{La}_{2-x}\text{Ce}_x\text{CuO}_4$, *npj Quantum Materials* **5**, 4 (2020).

[42] M. Hepting, M. Bejas, A. Nag, H. Yamase, N. Coppola, D. Betto, C. Falter, M. Garcia-Fernandez, S. Agrestini, K.-J. Zhou, M. Minola, C. Sacco, L. Maritato, P. Orgiani, H. I. Wei, K. M. Shen, D. G. Schlom, A. Galdi, A. Greco, and B. Keimer, Gapped collective charge excitations and interlayer hopping in cuprate superconductors, *Physical Review Letters* **129**, 047001 (2022).

[43] A. Singh, H. Y. Huang, C. Lane, J. H. Li, J. Okamoto, S. Komiya, R. S. Markiewicz, A. Bansil, A. Fujimori, C. T. Chen, and D. J. Huang, Acoustic plasmons and conducting carriers in hole-doped cuprate superconductors, *Physical Review B* **105**, 235105 (2022), arXiv:2006.13424 [cond-mat].

[44] M. Hepting, T. D. Boyko, V. Zimmermann, M. Bejas, Y. E. Suyolcu, P. Puphal, R. J. Green, L. Zinni, J. Kim, D. Casa, M. H. Upton, D. Wong, C. Schulz, M. Bartkowiak, K. Habicht, E. Pomjakushina, G. Cristiani, G. Logvenov, M. Minola, H. Yamase, A. Greco, and B. Keimer, Evolution of plasmon excitations across the phase diagram of the cuprate superconductor $\text{La}_{2-x}\text{Sr}_x\text{CuO}_4$, *Physical Review B* **107**, 214516 (2023).

[45] M. Bejas, V. Zimmermann, D. Betto, T. D. Boyko, R. J. Green, T. Loew, N. B. Brookes, G. Cristiani, G. Logvenov, M. Minola, B. Keimer, H. Yamase, A. Greco, and M. Hepting, Plasmon dispersion in bilayer cuprate superconductors, *Physical Review B* **109**, 144516 (2024).

[46] A. Nag, L. Zinni, J. Choi, J. Li, S. Tu, A. C. Walters, S. Agrestini, S. M. Hayden, M. Bejas, Z. Lin, H. Yamase, K. Jin, M. García-Fernández, J. Fink, A. Greco, and K.-J. Zhou, Impact of electron correlations on two-particle charge response in electron- and hole-doped cuprates, *Physical Review Research* **6**, 043184 (2024).

[47] J. Levallois, M. K. Tran, D. Pouliot, C. N. Presura, L. H. Greene, J. N. Eckstein, J. Uccelli, E. Giannini, G. D. Gu, A. J. Leggett, and D. van der Marel, Temperature-dependent ellipsometry measurements of partial Coulomb energy in superconducting cuprates, *Physical Review X* **6**, 031027 (2016).

[48] J. Zhang, A. Botana, J. Freeland, D. Phelan, H. Zheng, V. Pardo, M. Norman, and J. Mitchell, Large orbital polarization in a metallic square-planar nickelate, *Nature Physics* **13**, 864 (2017).

[49] J. Zhang, Y.-S. Chen, D. Phelan, H. Zheng, M. R. Norman, and J. F. Mitchell, Stacked charge stripes in the quasi-2D trilayer nickelate $\text{La}_4\text{Ni}_3\text{O}_8$, *Proceedings of the National Academy of Sciences* **113**, 8945 (2016).

[50] J. Zhang, D. M. Pajerowski, A. S. Botana, H. Zheng, L. Harriger, J. Rodriguez-Rivera, J. P. C. Ruff, N. J. Schreiber, B. Wang, Y.-S. Chen, W. C. Chen, M. R. Norman, S. Rosenkranz, J. F. Mitchell, and D. Phelan, Spin stripe order in a square planar trilayer nickelate, *Physical Review Letters* **122**, 247201 (2019).

[51] H. Li, P. Hao, J. Zhang, K. Gordon, A. G. Linn, X. Chen, H. Zheng, X. Zhou, J. F. Mitchell, and D. S. Dessau, Electronic structure and correlations in planar trilayer nickelate $\text{Pr}_4\text{Ni}_3\text{O}_8$, *Science Advances* **9**, eade4418 (2023).

[52] H. Yamase, Theory of charge dynamics in bilayer electron system with long-range Coulomb interaction, *Physical Review B* **111**, 085138 (2025).

[53] N. Sellati and L. Benfatto, Ghost Josephson plasmon in bilayer superconductors, *Physical Review B* **111**, 104509 (2025).

[54] S. Huangfu, Z. Guguchia, D. Cheptiakov, X. Zhang, H. Luetkens, D. J. Gawryluk, T. Shang, F. O. von Rohr, and A. Schilling, Short-range magnetic interactions and spin-glass behavior in the quasi-two-dimensional nickelate $\text{Pr}_4\text{Ni}_3\text{O}_8$, *Physical Review B* **102**, 054423 (2020).

[55] E. M. Nica, J. Krishna, R. Yu, Q. Si, A. S. Botana, and O. Erten, Theoretical investigation of superconductivity in trilayer square-planar nickelates, *Physical Review B* **102**, 020504 (2020).

[56] J. Karp, A. Hampel, M. Zingl, A. S. Botana, H. Park, M. R. Norman, and A. J. Millis, Comparative many-body study of $\text{Pr}_4\text{Ni}_3\text{O}_8$ and NdNiO_2 , *Physical Review B* **102**, 245130 (2020).

[57] M. Mitrano, A. A. Husain, S. Vig, A. Kogar, M. S. Rak, S. I. Rubeck, J. Schmalian, B. Uchoa, J. Schneeloch, R. Zhong, G. D. Gu, and P. Abbamonte, Anomalous density fluctuations in a strange metal, *Proceedings of the National Academy of Sciences* **115**, 5392 (2018).

[58] A. A. Husain, M. Mitrano, M. S. Rak, S. Rubeck, B. Uchoa, K. March, C. Dwyer, J. Schneeloch, R. Zhong, G. D. Gu, and P. Abbamonte, Crossover of charge fluctuations across the strange metal phase diagram, *Phys. Rev. X* **9**, 041062 (2019).

[59] A. Romero-Bermúdez, A. Krikun, K. Schalm, and J. Zaanen, Anomalous attenuation of plasmons in strange metals and holography, *Physical Review B* **99**, 235149 (2019).

[60] G. Paasch, Influence of interband transitions on plasmons in the alkali metals; pseudopotential calculation, *physica status solidi (b)* **38**, A123 (1970).

[61] A. J. Leggett, Cuprate superconductivity: Dependence of T_c on the c -axis layering structure, *Physical Review Letters* **83**, 392 (1999).

[62] I. Božović, Atomic-layer engineering of superconducting oxides: yesterday, today, tomorrow, *IEEE Transactions on Applied Superconductivity* **11**, 2686 (2001).

[63] M. Dean, R. Springell, C. Monney, K. Zhou, J. Pereiro, I. Božović, B. Dalla Piazza, H. Rønnow, E. Morenzoni, J. Van Den Brink, *et al.*, Spin excitations in a single La_2CuO_4 layer, *Nature Materials* **11**, 850 (2012).

[64] M. Dean, G. Dellea, R. Springell, F. Yakhou-Harris, K. Kummer, N. Brookes, X. Liu, Y. Sun, J. Strle, T. Schmitt, *et al.*, Persistence of magnetic excitations in $\text{La}_{2-x}\text{Sr}_x\text{CuO}_4$ from the undoped insulator to the heavily overdoped non-superconducting metal, *Nature Materials* **12**, 1019 (2013).

[65] D. Meyers, H. Miao, A. C. Walters, V. Bisogni, R. S. Springell, M. d'Astuto, M. Dantz, J. Pelliciari, H. Y. Huang, J. Okamoto, D. J. Huang, J. P. Hill, X. He, I. Božović, T. Schmitt, and M. P. M. Dean, Doping dependence of the magnetic excitations in $\text{La}_{2-x}\text{Sr}_x\text{CuO}_4$, *Physical Review B* **95**, 075139 (2017).

Supplemental Material: Observation of correlated plasmons in low-valence nickelates

Y. Shen[✉], W. He[✉], J. Sears[✉], Xuefei Guo[✉], Xiangpeng Luo[✉], A. Roll[✉], J. Li[✉], J. Pelliciari[✉], Xi He[✉], I. Božović[✉], Junjie Zhang[✉], J. F. Mitchell[✉], V. Bisogni[✉], M. Mitrano[✉], S. Johnston[✉], and M. P. M. Dean^{✉†}

(Dated: January 21, 2026)

CONTENTS

S1. Resonant behaviors of plasmons	1
S2. Fitting of the RIXS spectra	2
References	7

S1. RESONANT BEHAVIORS OF PLASMONS

The overdoped low-valence nickelates $R_4Ni_3O_8$ exhibit a pre-peak feature in the O K -edge XAS [1], indicative of an appreciable amount of ligand holes and nonzero Ni-O hybridization. Figure S1 depicts the RIXS energy map measured on $Pr_4Ni_3O_8$ single crystals, which shows multiple Raman-like features resonant at the pre-peak regime, indicating various excitations. As revealed in our prior studies, the high-energy strong features correspond to charge-transfer excitations, and the lower-energy weak features originate from dd excitations through Ni-O hybridization. Plasmons are observed with lower energy loss (~ 0.2 eV), which is absent in the insulating phase of $La_4Ni_3O_8$ [2]. Its resonant behavior highlights the localized characters.

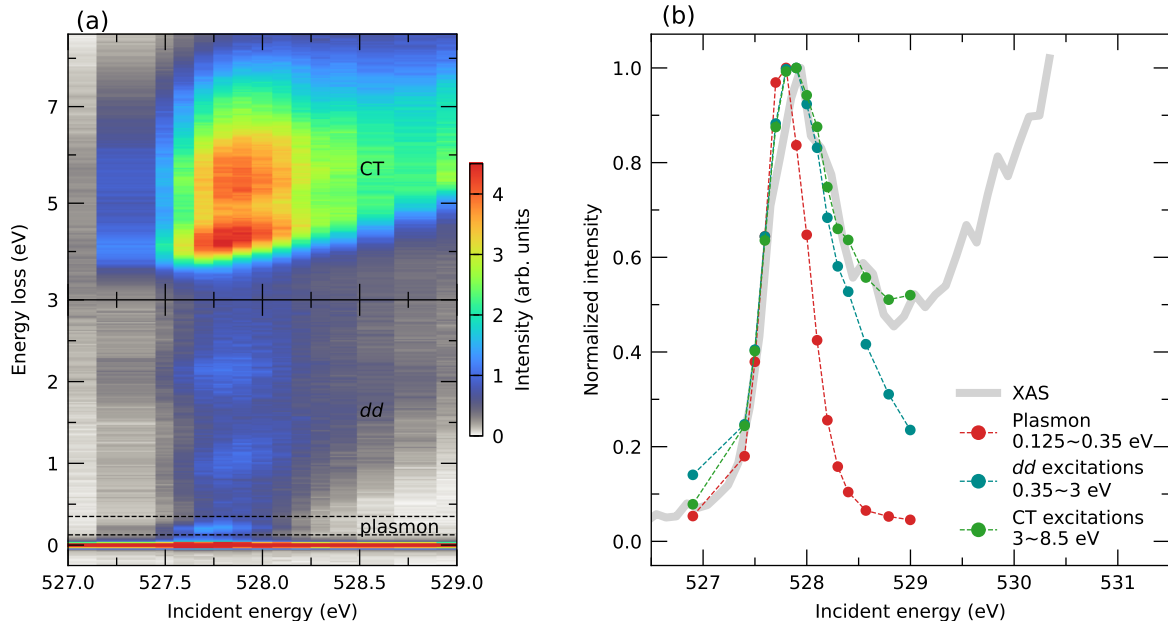


FIG. S1. Energy dependent resonant inelastic x-ray scattering (RIXS) spectra. (a), RIXS energy maps across the pre-edge regime of the O K edge collected with $\theta=22.6^\circ$ and σ polarization. Various excitations are identified, including the charge-transfer (CT) excitations, orbital dd excitations, and plasmons. Additionally, weak phonons are observed overlapping with the quasi-elastic peak. The XAS data were collected in partial fluorescence yield (PFY) mode. (b), Incident energy dependence of the RIXS spectral weights integrated in the indicated energy ranges, representing different excitations.

* yshen@iphy.ac.cn

† mdean@bnl.gov

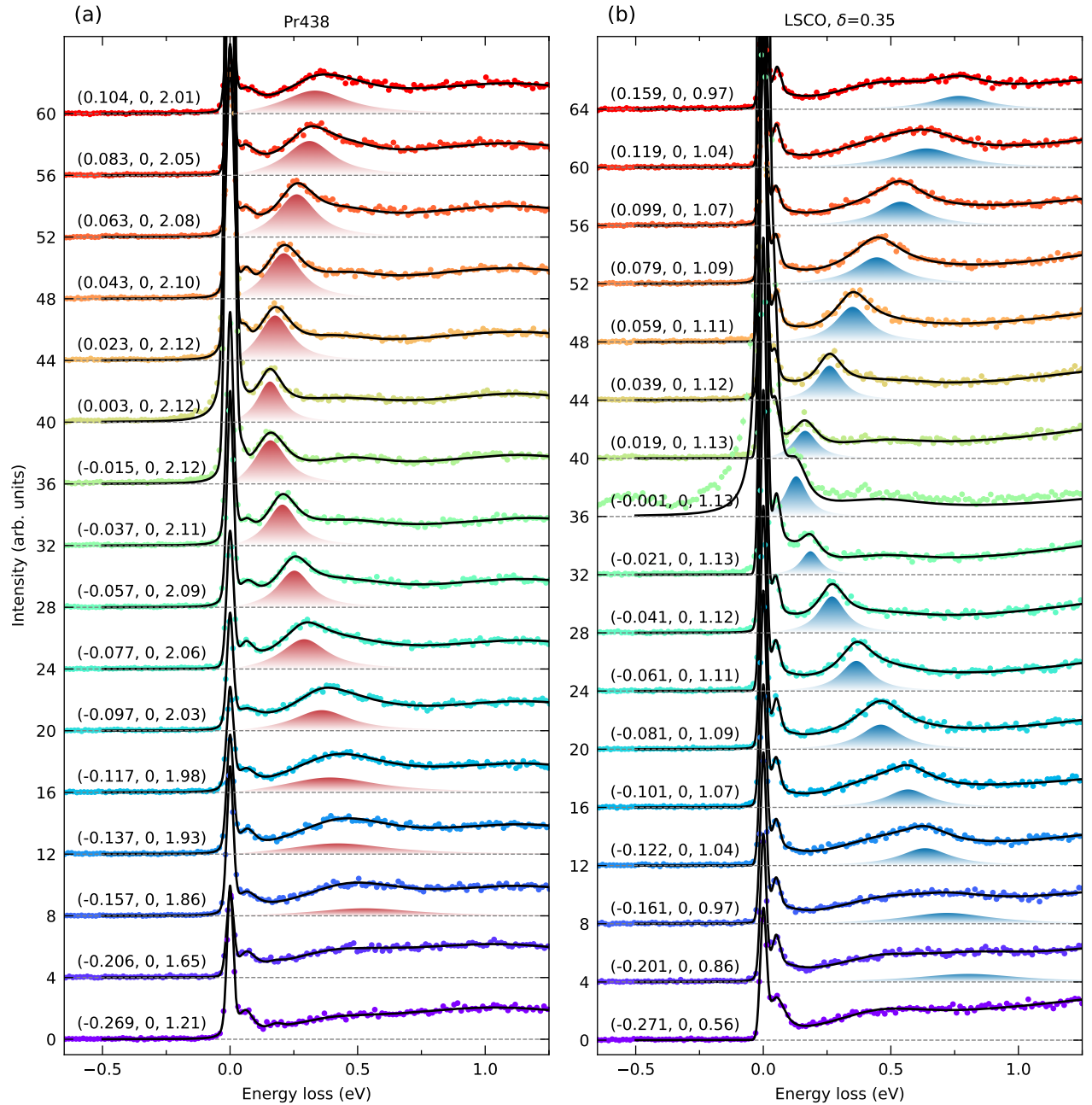


FIG. S2. Background subtracted O K -edge RIXS spectra for the in-plane plasmon dispersions. All the data for $\text{Pr}_4\text{Ni}_3\text{O}_8$ (Pr438) and $\text{La}_{2-x}\text{Sr}_x\text{CuO}_4$ (LSCO) were measured at 40 K. The dots present the data collected at the indicated \mathbf{Q} positions, and the solid lines are fitting results. The shaded areas highlight the plasmon contributions.

S2. FITTING OF THE RIXS SPECTRA

Figure S2 and Fig. S3 present the RIXS spectra for plasmon dispersions along the in-plane and out-of-plane directions, respectively. A constant background has been subtracted for all the spectra using the energy-gain side. For $\text{Pr}_4\text{Ni}_3\text{O}_8$, each spectrum was fit with five components, including a pseudo-Voigt profile, representing the quasi-elastic peak, and four damped harmonic oscillators convoluted with resolution functions determined by the quasi-elastic peak to account for the phonons at ~ 0.08 eV, dispersive plasmons indicated by the shaded areas, and two high-energy dd excitation modes. For $\text{La}_{2-x}\text{Sr}_x\text{CuO}_4$, we consider two phonon modes, one dispersionless bimagnon branch, and a tail from higher-energy charge excitations.

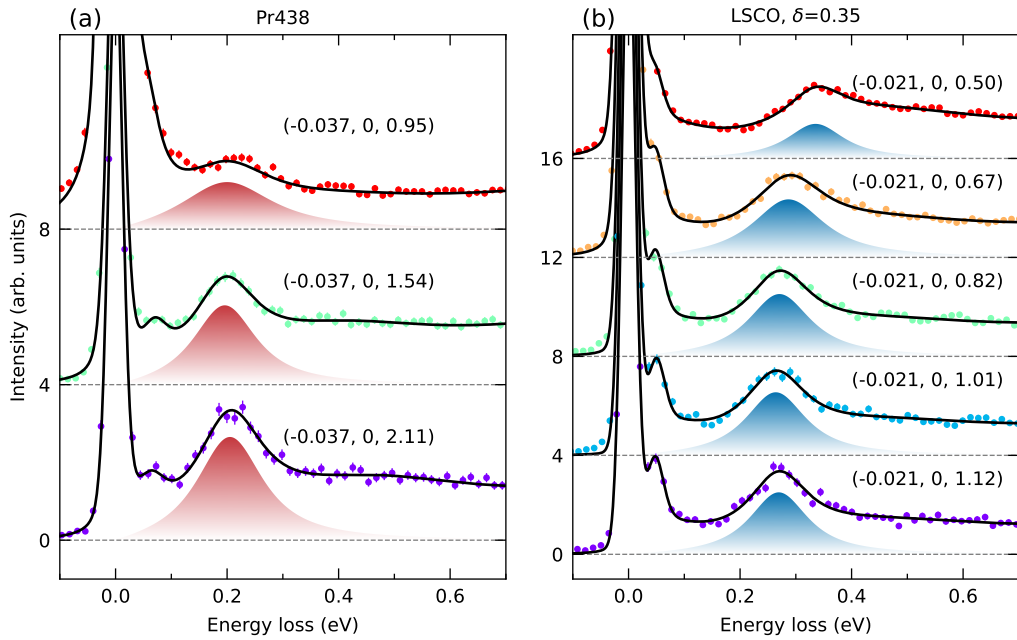


FIG. S3. RIXS spectra along the the out-of-plane direction.

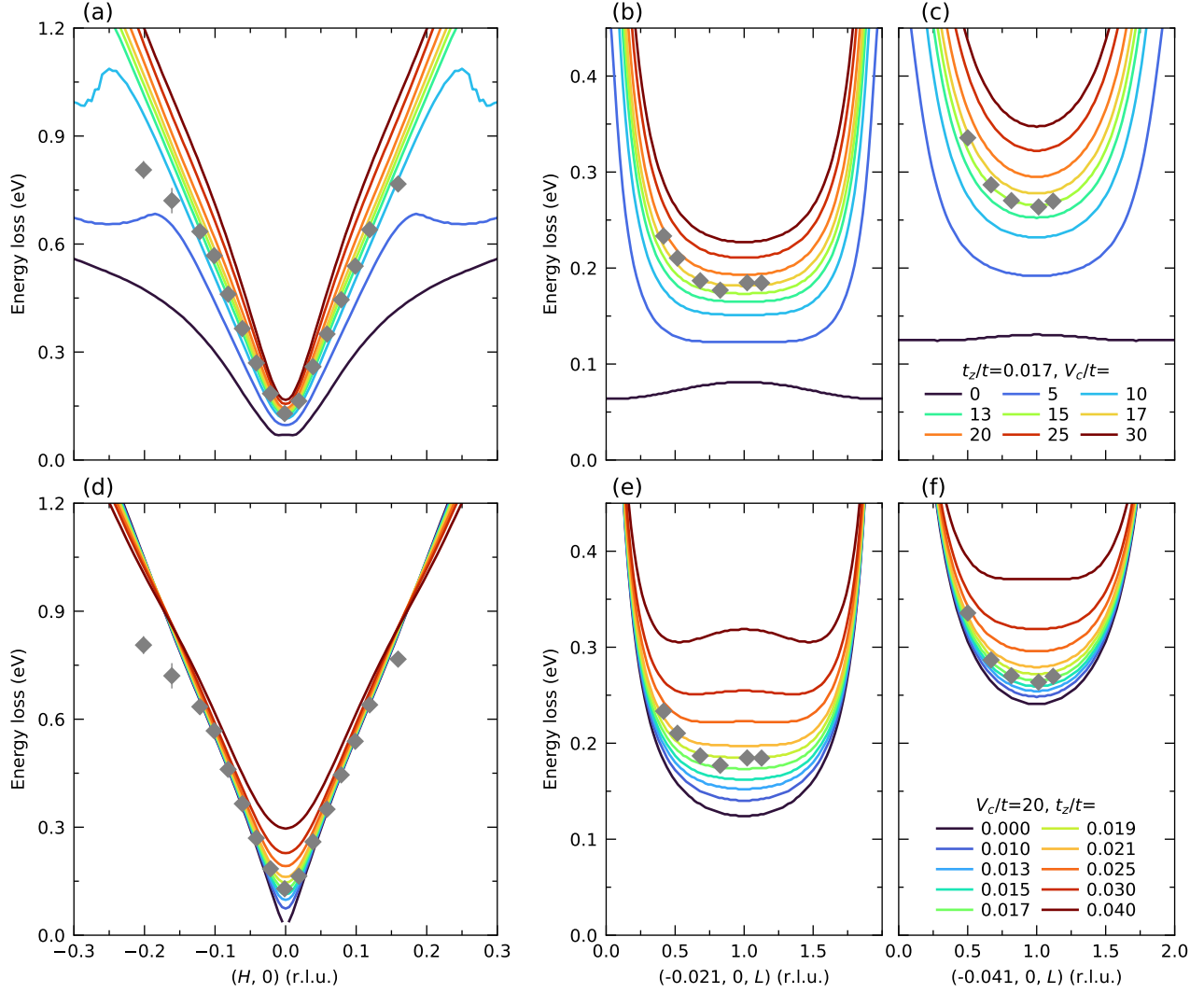


FIG. S4. random phase approximation (RPA) calculations of $\text{La}_{2-x}\text{Sr}_x\text{CuO}_4$ ($\delta=0.35$) plasmons with tuning parameters. The diamonds are data points, and the solid lines are calculation results.

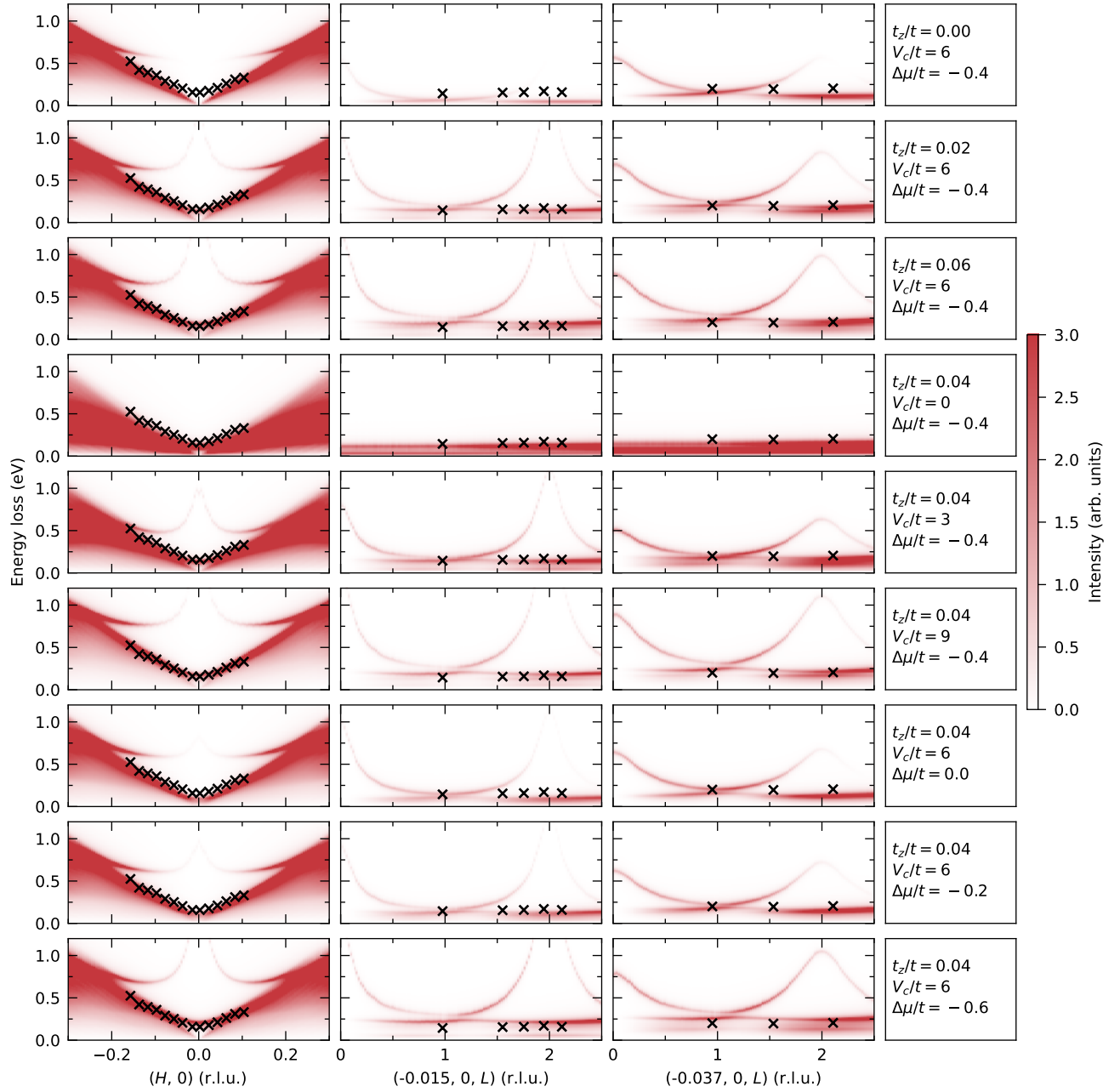


FIG. S5. RPA calculations of $\text{Pr}_4\text{Ni}_3\text{O}_8$ plasmons with tuning parameters. The crossings are data points.

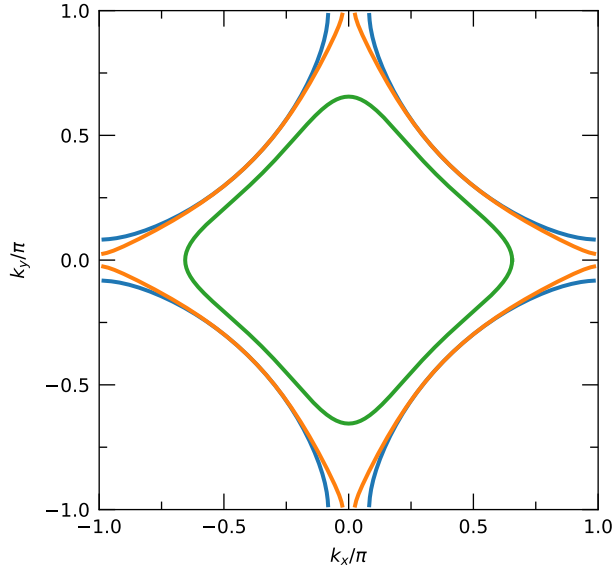


FIG. S6. Calculated $\text{Pr}_4\text{Ni}_3\text{O}_8$ Fermi surface using the parameters in the main text.

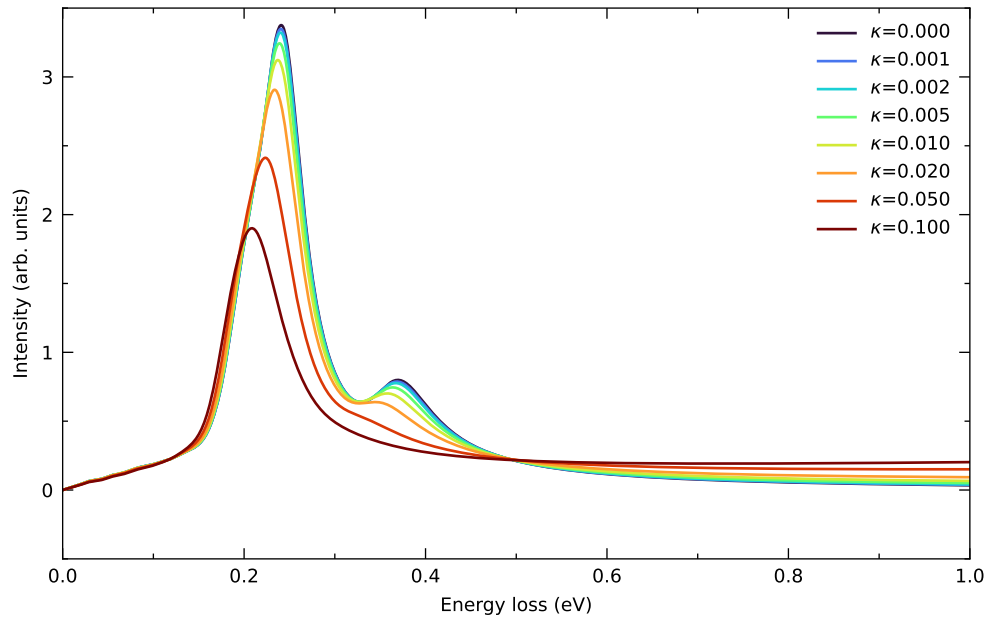


FIG. S7. RPA calculations of $\text{Pr}_4\text{Ni}_3\text{O}_8$ plasmons with various self-energy broadenings.

- [1] Junjie Zhang, AS Botana, JW Freeland, D Phelan, Hong Zheng, V Pardo, MR Norman, and JF Mitchell, “Large orbital polarization in a metallic square-planar nickelate,” *Nature Physics* **13**, 864–869 (2017).
- [2] Y. Shen, J. Sears, G. Fabbri, J. Li, J. Pelliciari, I. Jarrige, Xi He, I. Božović, M. Mitrano, Junjie Zhang, J. F. Mitchell, A. S. Botana, V. Bisogni, M. R. Norman, S. Johnston, and M. P. M. Dean, “Role of oxygen states in the low valence nickelate $\text{La}_4\text{Ni}_3\text{O}_8$,” *Physical Review X* **12**, 011055 (2022).